ROYAL SOCIETY
OF CHEMISTRY

CrossMark
← click for updates

Formation of Li_3O_4 nano particles in the discharge products of non-aqueous lithium–oxygen batteries leads to lower charge overvoltage†

L. Shi, A. Xu and T. S. Zhao*

Density functional theory calculations are made for bulk thermodynamic properties and surface energies of Li_2O_2, a primary discharge product, and Li_3O_4, a possible byproduct in the discharge products, of the non-aqueous lithium–oxygen batteries. Results show that the standard formation Gibbs free energy of bulk Li_3O_4 is marginally higher than that of Li_2O_2, but the surface energy of Li_3O_4 is much lower. Low surface energy results in both lowered nucleation energy and formation Gibbs free energy in the nano-meter regime, allowing the Li_3O_4 nano particles to nucleate ahead of Li_2O_2 during the discharge process and to exist stably when particle sizes are smaller than about 40 nm. The scanning transmission electron microscopy (STEM) image of Li_3O_4 crystals is simulated and compared with the measured STEM image of the discharge product particles. The consistency between the simulated and measured STEM images suggests that the Li_3O_4 phase can exist stably as a discharge product. The energy profile of the oxygen evolution reaction (OER) occurring on the most abundant surfaces of Li_3O_4 is also calculated. The predicted overpotential for the OER on the {0001} surface (0.30 V) shows a good agreement with experimental data. The presence of more electronically conductive Li_3O_4 nano particles in the primary discharge product Li_2O_2 tends to decrease the charge overvoltage of the batteries, explaining why the lower voltage area (<3.5 V) was widely observed during the charging of the batteries. An increase in the oxygen pressure or a decrease in temperature enhances the stability of the Li_3O_4 phase and increase the proportion of the Li_3O_4 phase in the discharge products, consequently leading to a lower overall charge overvoltage.

1. Introduction

As one of the most promising candidates to replace conventional lithium-ion batteries, non-aqueous lithium–oxygen batteries have attracted increasing attention because of their super-high specific capacity.[1–6] However, our understanding toward this novel battery system is still quite limited.[7] For instance, while it is now widely agreed that Li_2O_2 is the primary discharge product of the batteries,[1–6] the charge profiles of the said discharge products vastly differ from that of the commercial Li_2O_2.[8] Commercial Li_2O_2 is an insulator and exhibits a constant charge voltage at about 3.6 V,[8] while the reported charge curves of non-aqueous lithium–oxygen batteries are varied,[9–12] most of which shared a significant fraction of area with charge voltage lower than 3.5 V. Identifying the reasons for a low charge voltage area will not only deepen our understanding toward the underlying working mechanisms of the battery system,

but will also point out possible ways to lower the overall charge voltage, and consequently enhance the battery's energy conversion efficiency.

Efforts have been made to understand the charge behavior of non-aqueous lithium–oxygen batteries, particularly on the origin of the lower charge voltage area. Radin and Siegeil[13] explained the charge behavior by examining the discharge product morphology, and attributing the lower charge voltage to Li_2O_2 decomposition in a thin-film morphology with thickness smaller than about 10 nm. According to this explanation, however, the charge voltage is expected to drop back down at the end of the charging process when the discharge product is thinner than 10 nm, contradictory to most experimental observations.[1–6] Kang et al.[14] proposed that the decomposition of Li_2O_2 followed a facile topotactic delithiation mechanism, which occurred at about 3.3 V, but failed to offer an explanation at the higher charge voltage area. Zhai et al.[11,15,16] and Xia et al.[17] proposed that the lower charge voltage was caused by the decomposition of a so-called "LiO_2-like" component, which possesses a better electronic conductivity than Li_2O_2 and has a tendency to reside at the outer part of the discharge product particles. However, the detailed structure and related thermodynamic properties of

Department of Mechanical and Aerospace Engineering, The Hong Kong University of Science and Technology, Clear Water Bay, Kowloon, Hong Kong SAR, China. E-mail: metzhao@ust.hk; Tel: +852 2358 8647

† Electronic supplementary information (ESI) available. See DOI: 10.1039/c5cp03886c

the "LiO$_2$-like" components are unknown, rendering this explanation less persuasive and preventing us from creating appropriate conditions to increase the proportion of "LiO$_2$-like" components in the discharge products.

Many possible structures of the "LiO$_2$-like" components have been explored. LiO$_2$ crystals might be a natural choice, but they have only been observed at 4.2 K[18] and have been identified to be relatively unstable under standard conditions in comparison to the stability of Li$_2$O$_2$ and Li$_2$O.[19,20] In addition, Bryantsev et al.[21] have demonstrated that LiO$_2$ molecules and their aggregates in the gas phase can exist only at low temperatures. Das et al.[22] found that LiO$_2$ clusters with a planar-ring shape are thermodynamically more stable than LiO$_2$ radicals and may survive during the discharge process. Zhai et al.[16] proposed that the interfacial effects between the LiO$_2$ molecules and the electrolyte may help to stabilize the LiO$_2$ radicals.

In a recent study, Yang et al. identified Li$_3$O$_4$ as a new stable stoichiometry of Li–O compounds by applying a first-principles swarm structure search calculation.[23] They proposed that this conductive Li$_3$O$_4$ phase may compete with Li$_2$O$_2$ during the discharge process and be responsible for the lower charge voltage and the corresponding peaks in Raman and O K-edge spectra. However, whether this Li$_3$O$_4$ stoichiometry exists in the discharge products of non-aqueous lithium–oxygen batteries still needs to be further assessed.

In this work, we provide a comprehensive study of bulk thermodynamic properties of the newly reported Li$_3$O$_4$ stoichiometry and Li$_2$O$_2$ using density functional theory (DFT) calculation. Various oxygen overbinding correction criteria are applied to different oxidation states to achieve accurate results.[14,24,25] Surface energies are obtained to study the competition between Li$_3$O$_4$ and Li$_2$O$_2$ at the initial nucleation process and their nanoscale stability. The scanning transmission electron microscopy (STEM) image of Li$_3$O$_4$ crystals is simulated and compared with the measured STEM image of the discharge product particles in non-aqueous lithium–oxygen batteries. The energy profiles of the oxygen evolution reaction (OER) occurring on the most abundant surfaces of Li$_3$O$_4$ are also calculated.

2. Computational methodology

Total energies were calculated using the ABINIT[26–28] software package with the projector augmented-wave (PAW) method[29] and Perdew–Burke–Ernzerhof (PBE) generalized gradient approximation (GGA)[30] with spin polarization. The plane-wave basis with an energy cutoff of 20 Ha was used, in conjunction with the Monkhorst–Pack scheme[31] for k-point sampling. The spacing of the k-point mesh was set to be less than 0.05 Å^{-1}. For geometric optimization, all atoms were relaxed to a force tolerance of 0.02 eV Å^{-1} or less.

To evaluate the vibrational entropy in solid states, we performed phonon calculations using the response function method[32] implemented in the ABINIT software for Li$_2$O$_2$, Li$_3$O$_4$ and LiO$_2$ and the frozen phonon method[33] implemented in the PHONOPY[34] software for Li metal within the harmonic approximation.[35]

DFT calculation overbinds the oxygen molecule and leads to large errors when assessing the formation energies of oxides (O^{2-}), peroxides (O$_2^{2-}$) and superoxides (O$_2^-$).[36] For different oxidation states, the broken degrees of the double oxygen bond are also different, therefore various correction criteria should be applied to achieve more accurate results.[14,24,25] In this work, we calculated and applied the oxidation correction energy E_{oxd} in the spirit of Kang et al.[24] The formation energies of M$_x$O$_y$ obtained from DFT calculations were defined as:

$$\Delta E_{form}(0\ \text{K}) = E_{M_xO_y} - xE_M - \frac{y}{2}E_{O_2} \qquad (1)$$

By comparing $\Delta E_{form}(0\ \text{K})$ with the experimental formation enthalpy at 300 K and 1 atm, we obtain E_{oxd}, which corrects both the error of DFT calculations and the differences in energies between 0 and 300 K.[24] As only lithium oxide compounds were considered in our work, for O^{2-} and O$_2^{2-}$, we directly compared the calculated formation energies of Li$_2$O and Li$_2$O$_2$ with the experimental formation enthalpies of Li$_2$O and Li$_2$O$_2$. As there are no available experimental data for LiO$_2$ to account for O$_2^-$, we used the mean correction energy obtained from the other alkali metal superoxide compounds instead. The detailed values are listed in Table 1. After obtaining the correction energies, we calculated the formation enthalpies of Li$_x$O$_y$ from:

$$\Delta H_{form}(300\ \text{K}) = \Delta E_{form}(0\ \text{K}) - \frac{y}{2}E_{oxd} \qquad (2)$$

The chemical potential of oxygen gas dependent on the oxygen partial pressure and temperature was calculated using:

$$\mu_{O_2}(T, P_{O_2}) = E_{O_2}(0\ \text{K}) + \Delta H_{O_2}(T) - TS_{O_2}^{expt}(T)$$
$$+ k_B T \ln\left(P_{O_2}/P_{O_2}^0\right) \qquad (3)$$

where $E_{O_2}(0\ \text{K})$ is the total energy of oxygen calculated in DFT, $\Delta H_{O_2}(T)$ is the enthalpy change from 0 K to T, for which we used diatomic ideal gas approximation as $7/2k_B T$, $S_{O_2}^{expt}(T)$ is the entropy of oxygen at 1 atm and at different temperatures obtained from experiments,[37] and $P_{O_2}^0$ is set to be 1 atm.

The surface energies were calculated using the slab model adding the vacuum layers.[39,40] All the slabs are symmetrized and contain more than four repeating layers with a vacuum layer thicker than 10 Å to achieve convergence within 1 meV Å^{-2} for the surface energies. The surface energies were calculated by:

$$\gamma = \frac{1}{2A}\left[G_{slab} - N_{Li}\mu_{Li}^{bulk} - N_O\mu_O^{bulk}\right] \qquad (4)$$

Table 1   The oxygen overbinding correction for different oxidation states

Oxidation state	M$_x$O$_y$	ΔE_{form} (eV/O$_2$, 0 K)	ΔH_{exp} (eV/O$_2$, 300 K, 1 atm)	ΔE_{form} − ΔH_{exp} (eV/O$_2$)	E_{oxd} (eV/O$_2$)
O^{2-}	Li$_2$O	−9.32	−12.41[36]	3.09	3.09
O^{2-}	Li$_2$O$_2$	−5.32	−6.58[36]	1.26	1.26
O$_2^-$	NaO$_2$	−2.49	−2.70[36]	0.21	0.22
	KO$_2$	−2.73	−2.93[36]	0.20	
	RbO$_2$	−2.64	−2.90[38]	0.26	

where A is the area of one slab surface, G_{slab} is the total free energy of the slab supercell, N_{Li} and N_O are the numbers of lithium and oxygen atoms, μ_{Li}^{bulk} and μ_O^{bulk} are the chemical potentials of lithium and oxygen, respectively. The chemical potentials of Li_xO_y are correlated by:

$$x\mu_{Li}^{bulk} + y\mu_O^{bulk} = G_{Li_xO_y} \qquad (5)$$

The surface energies can be rewritten as:

$$\gamma = \frac{1}{2A}\left[G_{slab} - \frac{N_{Li}}{x}G_{Li_xO_y} + \left(\frac{N_{Li}y}{x} - N_O\right)\mu_O^{bulk}\right] \qquad (6)$$

The Wulff shapes were constructed using the WulffMaker software package.[41] The simulated STEM image was obtained from the QSTEM software package.[42]

The energy profiles of the OER occurring on abundant surfaces of Li_3O_4 were calculated using the above mentioned slab model. At each step, a lithium atom or an oxygen molecule was removed from the surface. All the removals were symmetrical on the both sides of the slab. The reaction free energy of intermediate steps was calculated by:

$$\Delta G = \frac{1}{2}\left[E_{slab}^{step} - E_{slab}^0 - \Delta N_O\mu_O^0 - \Delta N_{Li}(\mu_{Li}^0 - eU)\right] \qquad (7)$$

where E_{slab}^{step} is the free energy of the slab at each step, E_{slab}^0 is the free energy of the initial slab, ΔN_{Li} and ΔN_O are the number of lithium and oxygen atoms removed from the surface, respectively, μ_O^0 is the chemical potential of oxygen under standard conditions as defined in eqn (3), μ_{Li}^0 is the chemical potential of bulk lithium metal, and eU is added to account for the electron energy under applied potential U.

3. Results and discussion

3.1 Bulk Phase

To assess the thermodynamic stability of Li_3O_4 compared with the main discharge product Li_2O_2, we calculated the formation Gibbs free energies of these two phases under different conditions. The Li_2O_2 crystal structure proposed by Cota et al.[43] and the Li_3O_4 crystal structure predicted by Yang et al.[23] were adopted in our calculations. To make this work more comprehensive, we also considered the thermodynamic properties of pyrite LiO_2, which has been reported to be the most stable LiO_2 crystal structure in previous calculations.[14,19] The optimized crystal structures of these compounds are shown in Fig. 1.

The formation enthalpy of Li–O compounds at different temperatures is obtained from:

$$\Delta H_{form}(T) = \Delta E_{form}(0\,K) - \frac{y}{2}E_{oxd}$$
$$+ \left[E_{Li_xO_y}^{harm}(T) - xE_{Li}^{harm}(T) - \frac{y}{2}\Delta H_{O_2}(T)\right]$$
$$- \left[E_{Li_xO_y}^{harm}(300\,K) - xE_{Li}^{harm}(300\,K) - \frac{y}{2}\Delta H_{O_2}(300\,K)\right]$$
$$= \Delta H_{form}(300\,K) + \Delta\Delta H_{form}(T) - \Delta\Delta H_{form}(300\,K)$$
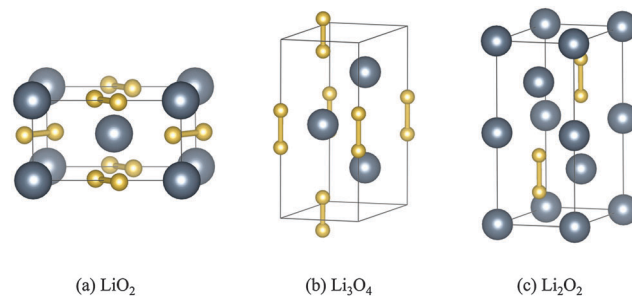$$(8)$$

(a) LiO₂   (b) Li₃O₄   (c) Li₂O₂

Fig. 1 Bulk crystal structure of *pnnm* LiO_2, $P\bar{6}m2$ Li_3O_4 and $P6_3/mmc$ Li_2O_2. The grey and yellow atoms correspond to lithium and oxygen respectively.

where $\Delta H_{form}(300\,K)$ is defined in eqn (2) and $\Delta\Delta H_{form}(T)$ is defined as:

$$\Delta\Delta H_{form}(T) \equiv E_{Li_xO_y}^{harm}(T) - xE_{Li}^{harm}(T) - \frac{y}{2}\Delta H_{O_2}(T) \qquad (9)$$

$E_i^{harm}(T)$ is the internal energy contributed from the phonon vibration. The formation Gibbs free energies were calculated using:

$$\Delta G_{form}(T,P_{O_2}) = \Delta H_{form}(T) - T\Delta S_{form}(T,P_{O_2}) \qquad (10)$$

where $\Delta S_{form}(T,P_{O_2})$ was approximated as:

$$\Delta S_{form}(T,P_{O_2}) = S_{Li_xO_y}^{harm} - xS_{Li}^{harm} - \frac{y}{2}S_{O_2}(T,P) \qquad (11)$$

S_i^{harm} is the entropy contributed from the phonon vibration and

$$S_{O_2}(T,P) = S_{O_2}^{expt}(T) - k_B\ln\left(P_{O_2}/P_{O_2}^0\right) \qquad (12)$$

The formation Gibbs free energies were compared in the unit of eV/Li. Under standard conditions, the calculated formation Gibbs free energy is −2.99 eV/Li for Li_2O_2, −2.97 eV/Li for Li_3O_4 and −2.91 eV/Li for LiO_2, corresponding to an equilibrium potential of 2.99 V, 2.97 V and 2.91 V, respectively. The phase diagram of these three compounds is shown in Fig. 2. From the bulk phase diagram, we find that Li_3O_4 is a transition metastable phase between LiO_2 and Li_2O_2. Under standard conditions, Li_2O_2 is the most stable phase, which agrees with the experimental observations that Li_2O_2 is the main discharge product.[1–6] By increasing the oxygen pressure or decreasing the temperature, Li_3O_4 will become more stable. LiO_2 is the most unstable phase and can only exist with low temperatures and high oxygen pressures.

3.2 Surface energies

To study the initial nucleation process and the phase stabilities of Li_3O_4 and Li_2O_2 at the nano scale, we take the influence of surface energy into our consideration.[24,44] Low-index surface energies for $P\bar{6}m2$ Li_3O_4 and $P6_3/mmc$ Li_2O_2 were calculated. We considered 4, 5 and 4 terminations for the {0001}, {11$\bar{2}$0} and {11$\bar{2}$1} surface orientations of Li_3O_4, respectively, and 2, 4, 3, 4, and 6 terminations for the {0001}, {11$\bar{2}$0}, {1$\bar{1}$00}, {11$\bar{2}$1} and {1$\bar{1}$20} surface orientations of Li_2O_2, respectively. The detailed structures and surface energies are provided in Fig. S3–S8 (ESI†).

This journal is © the Owner Societies 2015

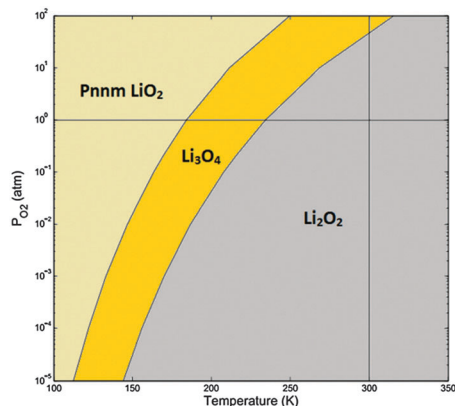*Phys. Chem. Chem. Phys.*, 2015, **17**, 29859–29866 | **29861**

Fig. 2 The bulk phase diagram of Li–O as a function of temperature and pressure, the grey domain indicates the stable region of $P6_3/mmc$ Li_2O_2, the dark yellow domain indicates the stable region of $P\bar{6}m2$ Li_3O_4, and the light yellow domain indicates the stable region of $Pnnm$ LiO_2. The horizontal and vertical solid line denote $P = 1$ atm and $T = 300$ K.
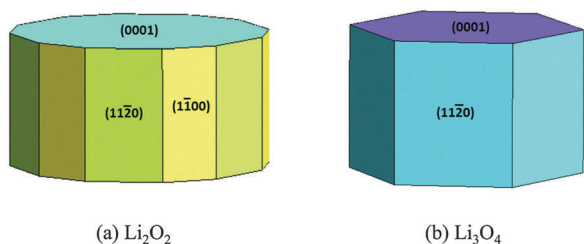

(a) Li_2O_2 (b) Li_3O_4

Fig. 3 The Wulff structure of Li_2O_2 and Li_3O_4 under standard conditions (300 K and 1 atm).

Fig. 3 shows the Wulff construction of Li_3O_4 and Li_2O_2 under standard conditions. The Wulff structure of Li_2O_2 showed a near cylindrical shape, which is in good agreement with the disc/toroid like discharge product particles reported elsewhere,[1–6,11,15,16] while the Wulff structure of Li_3O_4 showed a hexagonal prism shape.

The Wulff structures of Li_2O_2 and Li_3O_4 are different and varied under different oxygen chemical potentials, making it difficult to make direct comparison between the formation Gibbs free energies of nano particles with different particle sizes. Here we define a normalized surface energy $\bar{\gamma}$ following the approach of Kang *et al.*[24] as:

$$\bar{\gamma}(T, P_{O_2}) \equiv \sum_i \gamma_i(T, P_{O_2}) \cdot A_{1,i} \quad (13)$$

where γ_i is the surface energy of facet i, and $A_{1,i}$ is the surface area of facet i for a unit volume (1 Å³) Wulff shape. The normalized surface energies of both Li_2O_2 and Li_3O_4 as a function of oxygen chemical potential are shown in Fig. S9 (ESI†).

3.3 Initial nucleation process

To clarify the competition between Li_3O_4 and Li_2O_2 nano-particles at the initial nucleation stage during discharge, we accounted for the influence of the electrochemical potential ϕ and the oxygen pressure P_{O_2} as driving forces. The nucleation

Gibbs free energy for a Li_xO_y bulk crystal with unit volume can be written as:

$$\Delta G_v(T, P_{O_2}, \phi) = \frac{\Delta G_{form}^{Li_xO_y}(T, 1\,atm) + xF\phi - k_B T \ln P_{O_2}}{vol_{Li_xO_y}} \quad (14)$$

where $vol_{Li_xO_y}$ is the volume of Li_xO_y per formula unit. Subsequently, the formation Gibbs free energy of a particle with size d, where $d = V^{1/3}$, becomes:

$$\Delta G_{form}(d, T, P_{O_2}, \phi) = \Delta G_v(T, P_{O_2}, \phi) \cdot d^3 + \bar{\gamma} \cdot d^2 \quad (15)$$

when

$$\frac{\partial \Delta G_{form}(d, T, P_{O_2}, \phi)}{\partial d} = 0 \quad (16)$$

we can obtain the critical nucleus size d^* and the critical nucleation energy ΔG^* as:

$$d^* = -\frac{2\bar{\gamma}(T, P_{O_2})}{3\Delta G_v(T, P_{O_2}, \phi)} \quad (17a)$$

$$\Delta G^* = -\frac{4\bar{\gamma}(T, P_{O_2})^3}{27\Delta G_v(T, P_{O_2}, \phi)^2} \quad (17b)$$

Fig. 4 illustrates d^* and ΔG^* for Li_2O_2 and Li_3O_4 as a function of oxygen pressure with a discharge potential of 2.75 V, which is a commonly reported discharge voltage in experiments.[1–6] It is shown that when the oxygen pressure is higher than about 0.01 atm, the critical nucleation energy of Li_3O_4 will be lower than that of Li_2O_2. When the oxygen pressure is higher than 0.1 atm, the critical nucleus size of Li_3O_4 will be smaller than that of Li_2O_2. Thus, when ensuring sufficient oxygen supply, Li_3O_4 will be more likely to nucleate ahead of Li_2O_2 due to its lower critical nucleation energy barrier and smaller critical nucleus size.

When the discharge voltage is changed, the results at $P_{O_2} = 1$ atm are shown in Fig. 5. At a discharge voltage lower than about 2.94 V, the critical nucleation energy of Li_3O_4 will be lower than that of Li_2O_2. At a discharge voltage lower than 2.90 V, the critical nucleus size of Li_3O_4 will be smaller than that of Li_2O_2. Thus, our pervious conclusion that Li_3O_4 will nucleate ahead of Li_2O_2 is validated under a wide range of discharge voltages.

It should also be noted that although d^* and ΔG^* of Li_3O_4 are lower than those of Li_2O_2 under a wide range of oxygen pressures and discharge voltages, their values are relatively close, which means that the nucleation process is competitive and both phases have the chance to nucleate.

3.4 Nano-scale stability

From the above calculations, we can find that Li_3O_4 nano particles are likely to nucleate ahead of Li_2O_2 during the discharge process. To study the thermodynamic stability of these nano particles after nucleation, we define the formation energy for a particle with size d as:

$$\Delta G_{form}(d, T, P_{O_2}) = \Delta G_{form}^{bulk}(T, P_{O_2}) \cdot d^3 + \bar{\gamma}(T, P_{O_2}) \cdot d^2 \quad (18)$$

29862 | *Phys. Chem. Chem. Phys.*, 2015, **17**, 29859–29866

This journal is © the Owner Societies 2015

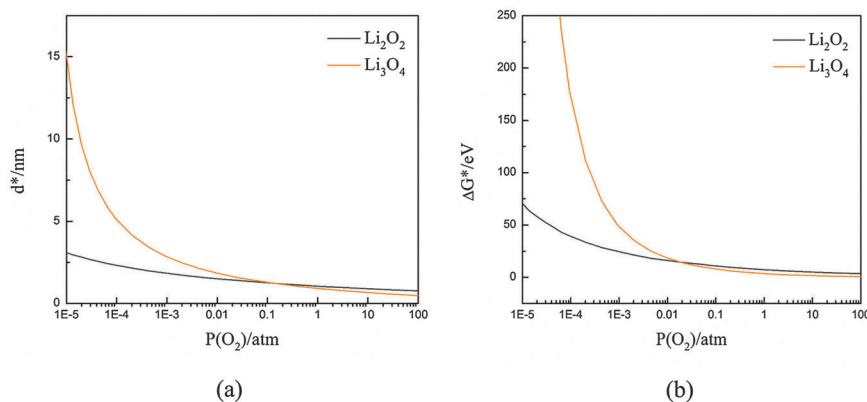(a)   (b)

Fig. 4   The critical nucleus size and the critical nucleation energy barrier of Li_3O_4 and Li_2O_2 as a function of oxygen pressure at φ = 2.75 V.
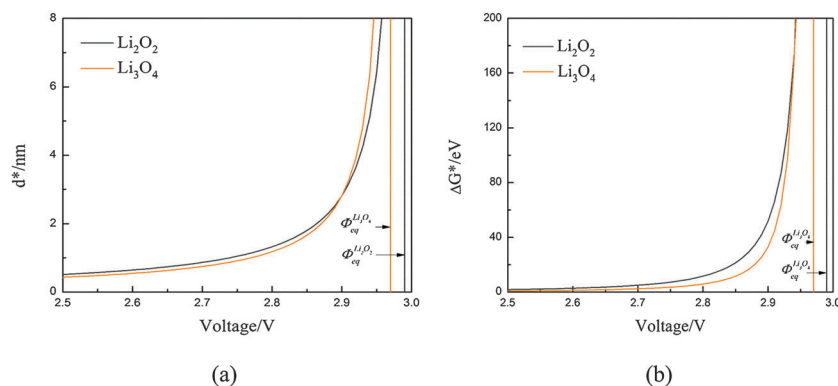

(a)   (b)

Fig. 5   The critical nucleus size and the critical nucleation energy barrier as a function of discharge voltage at P_{O_2} = 1 atm.

Here, $\Delta G_{form}^{bulk}(T, P_{O_2})$ is defined as the formation energy of bulk crystals in unit volume. To make a reasonable comparison, we compared the formation Gibbs free energies between the Li_3O_4 and Li_2O_2 nano particles with the same number of lithium atoms. The resulting phase diagram at 300 K is shown in Fig. 6, where d is the size of Li_2O_2 nanoparticles. To convert it to the size of Li_3O_4 particles, we can use:

$$d_{Li_3O_4} = d_{Li_2O_2} \cdot \left(\frac{4 vol_{Li_3O_4}}{3 vol_{Li_2O_2}} \right)^{\frac{1}{3}} \quad (19)$$

where $vol_{Li_3O_4}$ and $vol_{Li_2O_2}$ are the volumes of the unit formula of Li_3O_4 and Li_2O_2 respectively. Substituting with the optimized lattice parameters of Li_3O_4 and Li_2O_2 in this work (listed in Table S2, ESI†), we obtain $d_{Li_3O_4} \approx 1.08 d_{Li_2O_2}$. For the Li_3O_4 and Li_2O_2 particles with the same number of lithium atoms, their sizes are similar.

Shown in Fig. 6, the Li_3O_4 phase is more stable when the particle size is smaller than about 40 nm at P_{O_2} = 1 atm. By increasing the oxygen pressure, the size of stable Li_3O_4 nano particles becomes larger. Thus, the nucleated Li_3O_4 nano particles are likely to stay in the discharge product due to their thermodynamic stability.

With the above results, the competition for nucleation between Li_2O_2 and Li_3O_4 during the discharge process is clear. Li_3O_4 is limited by its bulk thermodynamic stability and can
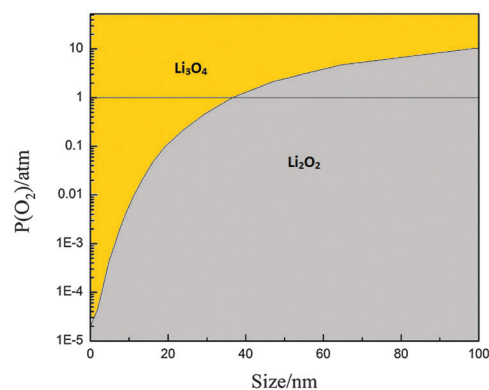

Fig. 6   The nano-scale phase diagram of Li_3O_4/Li_2O_2. The grey domain indicates the stable region for Li_2O_2, and the dark yellow domain indicates the stable region for Li_3O_4. The horizontal line denotes P_{O_2} = 1 atm.

only exist in its stable form as nanoparticles. Some of these Li_3O_4 nanoparticles may reside at the outer part of the discharge product particles between the layers of Li_2O_2 crystallites,[11] disrupting the crystallization process of Li_2O_2 particles and inducing a toroidal morphology. On the other hand, while the initial nucleation process for Li_2O_2 may occur a little later, the particles will grow to larger sizes and will continue to grow, eventually becoming the main phase.
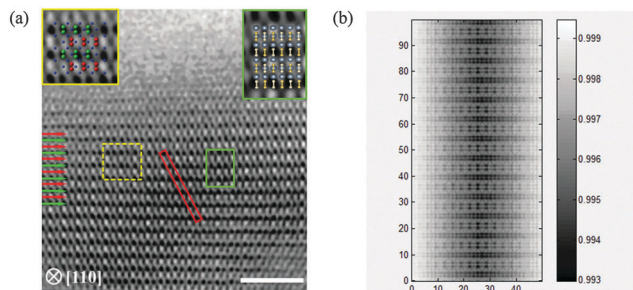
This journal is © the Owner Societies 2015

Phys. Chem. Chem. Phys., 2015, **17**, 29859–29866 | **29863**

Fig. 7 (a) The STEM image of the outer part of the discharge product particles of non-aqueous lithium–oxygen battery along the (110) zone axis,[45] the picture in the top left yellow rectangle is Xiao *et al.*'s explanation as Li_2O_2 with oxygen deficiency (the green and red spheres represent the oxygen atoms in perfect and defective LiO_2 layer, respectively, the dark blue spheres indicate the lithium atoms) and the picture in the top right green rectangle is our explanation as Li_3O_4 (the grey spheres represent lithium atoms, the light yellow spheres represent oxygen atoms in the upper layer and the dark yellow spheres represent oxygen atoms in the lower layer). The scale bar is 3 nm (b) the simulated STEM image of the Li_3O_4 ($1\bar{1}0$) surface, the unit of the coordinates is angstrom.

3.5 STEM simulation

We performed a STEM simulation on the $Li_3O_4\{1\bar{1}00\}$ surface ([110] zone axis) and compared it with the measured STEM image reported by Xiao *et al.*[45] The simulation results are shown in Fig. 7b. It is found that the size of the unit cell (~ 3.2 Å $\times$ 7.4 Å) and the patterns of the image match well with the experimental results. Xiao *et al.* explained the line of a single dark spot in the STEM image as the oxygen-deficient layer in Li_2O_2 crystals, as shown in the yellow rectangle in Fig. 7a. We offer the alternative explanation that the dark spot is attributed as the row of oxygen dimer in the Li_3O_4 crystal structure without lithium atoms, as shown in the green rectangle in Fig. 7a. As the STEM image was taken from the outer part of the discharge product particles, the assumption of the observed crystal structure to be Li_3O_4 agrees well with previous reports that the "LiO_2-like" components reside at the outer part of the discharge product.[11,15–17]

3.6 Proposed charge mechanism

Under standard conditions, Li_3O_4 is more likely to nucleate ahead of Li_2O_2 at the initial stage of the discharge process and

continue to grow to about 40 nm because of its nano-scale stability. As the Li_3O_4 nano particles are thermodynamically stable, they may reside at the outer part of discharge product particles between the Li_2O_2 crystal plates and act as the "LiO_2-like" component[11,15–17] or stay on the surface of cathode substrates, as illustrated in Fig. 9(a).

To gain a deeper understanding about the OER occurring on the surface of Li_3O_4, we calculated the energy profiles of the OER occurring on the $\{0001\}$ and $\{11\bar{2}0\}$ surfaces of Li_3O_4. The energy profiles of the lowest energy path under equilibrium potential $U = 2.97$ V are shown in Fig. 8. The minimum energy barriers for the OER are 0.30 V for the $\{0001\}$ surface and 1.32 V for the $\{11\bar{2}0\}$ surface. If considering the high energy surfaces or special configurations like kinks and steps, the minimum energy barrier may be further lowered.[46,47] During the realistic charging process, the OER will mainly take place at the surface with the lowest energy barrier. Thus, if we do not consider the ohmic resistance, the theoretical charge overpotentials for Li_3O_4 should be equal to or lower than 0.30 V, corresponding to a charge voltage equal to or lower than 3.27 V. The OER occurring on the low-index surfaces of Li_2O_2 has been discussed in detail by Mo *et al.*,[46] and the reported minimum energy barriers for the most abundant surfaces range from 0.27 to 0.61 V. In the situations where the ohmic resistance of Li_2O_2 can be ignored, the theoretical lowest charge voltage of Li_2O_2 is close to that of Li_3O_4.

As opposed to Li_2O_2, Li_3O_4 is a half metallic material[23] with better electronic conductivity. Thus, during the charge process, they are expected to be charged back at lower overvoltage compared with Li_2O_2 particles. Considering the previously reported superior lithium ion conductivity in amorphous Li_2O_2,[48] we propose the charge mechanism as shown in Fig. 9. The Li_3O_4 phase together with Li_2O_2 in thin film morphology (when the ohmic resistance can be ignored) will be decomposed at lower overvoltage (<3.5 V), followed by the decomposition of amorphous Li_2O_2 and Li_2O_2 nano particles. The decomposition of large Li_2O_2 particles requires higher overvoltage to activate the charge transport and is responsible for the charge voltage of around 4.0 V.[13] Finally, byproducts like lithium carboxylates, Li_2CO_3 and $LiOH$ will be decomposed at a voltage higher than 4.2 V.[49]
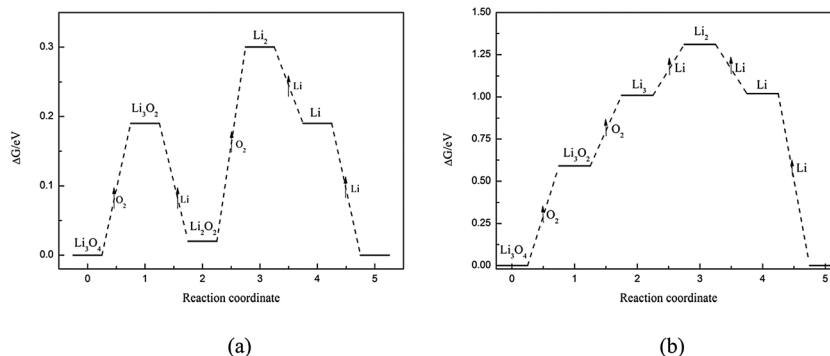

(a)

(b)

Fig. 8 The energy profile for OER on the (a) $\{0001\}$ surface and the (b) $\{11\bar{2}0\}$ surface of Li_3O_4 with $U = 2.97$ V (equilibrium potential), starting from the most stable termination.

29864 | *Phys. Chem. Chem. Phys.*, 2015, **17**, 29859–29866

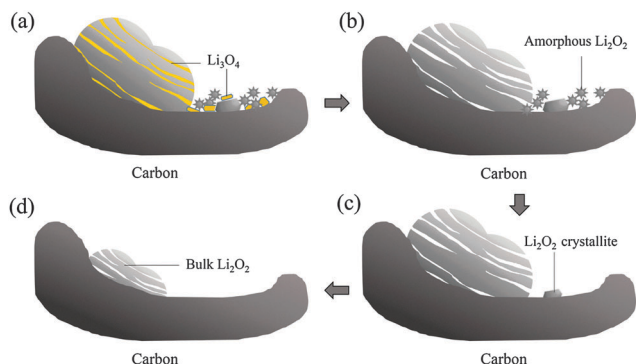This journal is © the Owner Societies 2015

Fig. 9 The proposed charge mechanism for non-aqueous lithium–oxygen batteries.

4. Conclusions

In this work, we have studied the bulk thermodynamic properties and surface energies of the primary discharge product, Li_2O_2, and the possible byproduct in the discharge products, Li_3O_4, of the non-aqueous lithium–oxygen batteries. The results show that the formation Gibbs free energy of Li_3O_4 is slightly higher than that of Li_2O_2, but its surface energy is much lower. The low surface energy results in low nucleation energy and low formation Gibbs free energy in the nanometer regime, allowing the Li_3O_4 nanoparticles to nucleate ahead of Li_2O_2 during the discharge process and to exist stably when particle sizes are smaller than about 40 nm. The scanning transmission electron microscopy (STEM) image of Li_3O_4 crystals is simulated and compared with the measured STEM image of the discharge product particles. The consistency between the simulated and measured STEM images suggests that the Li_3O_4 phase can exist stably as a discharge product. The OER reaction mechanisms occurring on $\{0001\}$ and $\{11\bar{2}0\}$ surfaces of Li_3O_4 were also investigated. An overpotential of 0.30 V for the OER on the $\{0001\}$ surface was predicted and showed good agreement with experimental data.[11,15,16]

As Li_3O_4 is electronically more conductive than Li_2O_2, its existence will favor a decrease in the charge overvoltage of the battery, explaining the wide observation of the low voltage area (<3.5 V). Increasing the oxygen pressure, decreasing the temperature or limiting the size of the discharge products to the nanoscale enhances the stability of the Li_3O_4 phase and increases the proportion of the Li_3O_4 phase in the discharge products, thus leading to a lower overall charge overvoltage.

Acknowledgements

References

1 A. C. Luntz and B. D. McCloskey, Nonaqueous Li–air batteries: a status report, *J. Chem. rev.*, 2014, **114**(23), 11721–11750.

2 M. Park, H. Sun and H. Lee, *et al.*, Lithium–Air Batteries: Survey on the Current Status and Perspectives Towards Automotive Applications from a Battery Industry Standpoint, *Adv. Energy Mater.*, 2012, **2**(7), 780–800.

3 J. Wang, Y. Li and X. Sun, Challenges and opportunities of nanostructured materials for aprotic rechargeable lithium–air batteries, *Nano Energy*, 2013, **2**(4), 443–467.

4 Z. Peng, S. A. Freunberger and Y. Chen, *et al.* A reversible and higher-rate Li–O₂ battery, *J. Sci.*, 2012, **337**(6094), 563–566.

5 M. A. Rahman, X. Wang and C. Wen, A review of high energy density lithium–air battery technology, *J. Appl. Electrochem.*, 2014, **44**(1), 5–22.

6 Y. C. Lu, B. M. Gallant and D. G. Kwabi, *et al.* Lithium–oxygen batteries: bridging mechanistic understanding and battery performance, *Energy Environ. Sci.*, 2013, **6**(3), 750–768.

7 L. Shi and T. Zhao, Why the charge overpotential in non-aqueous Li–O₂ batteries is so high and exhibits different rising trends? *Sci. Bull.*, 2014, 1–2.

8 S. Ganapathy, B. D. Adams and G. Stenou, *et al.*, Nature of Li₂O₂ oxidation in a Li–O₂ battery revealed by operando X-ray diffraction, *J. Am. Chem. Soc.*, 2014, **136**(46), 16335–16344.

9 B. D. McCloskey, A. Speidel and R. Scheffler, *et al.*, Twin problems of interfacial carbonate formation in nonaqueous Li–O₂ batteries, *J. Phys. Chem. Lett.*, 2012, **3**(8), 997–1001.

10 B. D. McCloskey, D. S. Bethune and R. M. Shelby, *et al.* Limitations in rechargeability of Li–O₂ batteries and possible origins, *J. Phys. Chem. Lett.*, 2012, **3**(20), 3043–3047.

11 D. Zhai, H. H. Wang and J. Yang, *et al.* Disproportionation in Li–O₂ batteries based on a large surface area carbon cathode, *J. Am. Chem. Soc.*, 2013, **135**(41), 15364–15372.

12 Y. C. Lu and Y. Shao-Horn, Probing the reaction kinetics of the charge reactions of nonaqueous Li–O₂ batteries, *J. Phys. Chem. Lett.*, 2012, **4**(1), 93–99.

13 M. D. Radin and D. J. Siegel, Charge transport in lithium peroxide: relevance for rechargeable metal–air batteries, *Energy Environ. Sci.*, 2013, **6**(8), 2370–2379.

14 S. Y. Kang, Y. Mo and S. P. Ong, *et al.* A facile mechanism for recharging Li₂O₂ in Li–O₂ batteries, *Chem. Mater.*, 2013, **25**(16), 3328–3336.

15 J. Yang, D. Zhai and H. H. Wang, *et al.* Evidence for lithium superoxide-like species in the discharge product of a Li–O₂ battery, *Phys. Chem. Chem. Phys.*, 2013, **15**(11), 3764–3771.

16 D. Zhai, K. C. Lau and H. H. Wang, *et al.* Interfacial Effects on Lithium Superoxide Disproportionation in Li–O₂ Batteries, *Nano Lett.*, 2015, **15**(2), 1041–1046.

17 C. Xia, M. Waletzko and L. Chen, *et al.* Evolution of Li₂O₂ Growth and Its Effect on Kinetics of Li–O₂ Batteries, *ACS Appl. Mater. Interfaces*, 2014, **6**(15), 12083–12092.

18 V. M. Bakulina and S. A. Tokareva, Vol'nov I I. X-Ray Diffraction Analysis of LiO₂, *Zh. Strukt. Khim.*, 1967, **8**(6), 1104–1105.

19 N. Seriani, *Ab initio* thermodynamics of lithium oxides: from bulk phases to nanoparticles, *Nanotechnology*, 2009, **20**(44), 445703.

20 K. C. Lau, L. A. Curtiss and J. Greeley, Density functional investigation of the thermodynamic stability of lithium

oxide bulk crystalline structures as a function of oxygen pressure, *J. Phys. Chem. C*, 2011, **115**(47), 23625–23633.

21 V. S. Bryantsev, M. Blanco and F. Faglioni, Stability of Lithium Superoxide LiO$_2$ in the Gas Phase: Computational Study of Dimerization and Disproportionation Reactions, *J. Phys. Chem. A*, 2010, **114**(31), 8165–8169.

22 U. Das, K. C. Lau and P. C. Redfern, *et al.* Structure and Stability of Lithium Superoxide Clusters and Relevance to Li–O$_2$ Batteries, *J. Phys. Chem. Lett.*, 2014, **5**(5), 813–819.

23 G. Yang, Y. Wang and Y. Ma, A Stable, Magnetic, and Metallic Li$_3$O$_4$ Compound as a Discharge Product in a Li–Air Battery, *J. Phys. Chem. Lett.*, 2014, **5**(15), 2516–2521.

24 S. Y. Kang, Y. Mo and S. P. Ong, *et al.* Nanoscale Stabilization of Sodium Oxides: Implications for Na–O$_2$ Batteries, *Nano Lett.*, 2014, **14**(2), 1016–1020.

25 L. Wang, T. Maxisch and G. Ceder, Oxidation energies of transition metal oxides within the GGA+U framework, *Phys. Rev. B: Condens. Matter Mater. Phys.*, 2006, **73**(19), 195107.

26 X. Gonze, J. M. Beuken and R. Caracas, *et al.* First-principles computation of material properties: the ABINIT software project, *Comput. Mater. Sci.*, 2002, **25**(3), 478–492.

27 X. Gonze, A brief introduction to the ABINIT software package, *Z. Kristallogr.*, 2005, **220**(5/6/2005), 558–562.

28 X. Gonze, B. Amadon and P. M. Anglade, *et al.* ABINIT: First-principles approach to material and nanosystem properties, *Comput. Phys. Commun.*, 2009, **180**(12), 2582–2615.

29 P. E. Blöchl, Projector augmented-wave method, *Phys. Rev. B: Condens. Matter Mater. Phys.*, 1994, **50**(24), 17953.

30 J. P. Perdew, K. Burke and M. Ernzerhof, Generalized gradient approximation made simple, *Phys. Rev. Lett.*, 1996, **77**(18), 3865.

31 H. J. Monkhorst and J. D. Pack, Special points for Brillouin-zone integrations, *Phys. Rev. B: Condens. Matter Mater. Phys.*, 1976, **13**(12), 5188.

32 X. Gonze, First-principles responses of solids to atomic displacements and homogeneous electric fields: implementation of a conjugate-gradient algorithm, *Phys. Rev. B: Condens. Matter Mater. Phys.*, 1997, **55**(16), 10337.

33 S. Wei and M. Y. Chou, *Ab initio* calculation of force constants and full phonon dispersions, *Phys. Rev. Lett.*, 1992, **69**(19), 2799.

34 A. Togo, F. Oba and I. Tanaka, First-principles calculations of the ferroelastic transition between rutile-type and CaCl$_2$-type SiO$_2$ at high pressures, *Phys. Rev. B: Condens. Matter Mater. Phys.*, 2008, **78**(13), 134106.

35 D. C. Wallace, *Thermodynamics of crystals*, Courier Corporation, 1998.

36 J. P. Perdew, S. Kurth and A. Zupan, *et al.* accurate density functional with correct formal properties: a step beyond the generalized gradient approximation, *Phys. Rev. Lett.*, 1999, **82**(12), 2544.

37 M. W. Chase, NIST-JANAF thermochemical tables, 1998.

38 R. H. Lamoreaux and D. L. Hildenbrand, High temperature vaporization behavior of oxides. I. Alkali metal binary oxides, *J. Phys. Chem. Ref. Data*, 1984, **13**(1), 151–173.

39 M. Ramamoorthy, R. D. King-Smith and D. Vanderbilt, Defects on TiO$_2$(110) surfaces, *Phys. Rev. B: Condens. Matter Mater. Phys.*, 1994, **49**(11), 7709.

40 K. ReuterM. Scheffler, Composition, structure and stability of RuO_2 (110) as a function of oxygen pressure, arXiv preprint cond-mat/0107229, 2001.

41 R. V. Zucker, D. Chatain and U. Dahmen, New software tools for the calculation and display of isolated and attached interfacial-energy minimizing particle shapes, *J. Mater. Sci.*, 2012, **47**(24), 8290–8302.

42 C. T. Koch, *Determination of Core Structure Periodicity and Point Defect Density along Dislocations*, PhD thesis, Arizona State University, 2002.

43 L. G. Cota and P. de la Mora, On the structure of lithium peroxide, Li$_2$O$_2$, *Acta Crystallogr., Sect. B: Struct. Sci.*, 2005, **61**(2), 133–136.

44 S. Bajaj, M. G. Haverty and R. Arroyave, *et al.* Phase stability in nanoscale material systems: extension from bulk phase diagrams, *Nanoscale*, 2015, **7**(21), 9868–9877.

45 D. Xiao, S. Dong and J. Guan, *et al.* Direct Observation of Ordered Oxygen Defects on the Atomic Scale in Li$_2$O$_2$ for Li–O$_2$ Batteries, *Adv. Energy Mater.*, 2015, **5**(3), 1400664.

46 Y. Mo, S. P. Ong and G. Ceder, First-principles study of the oxygen evolution reaction of lithium peroxide in the lithium–air battery, *Phys. Rev. B: Condens. Matter Mater. Phys.*, 2011, **84**(20), 205446.

47 J. S. Hummelshøj, A. C. Luntz and J. K. Nørskov, Theoretical evidence for low kinetic overpotentials in Li–O$_2$ electrochemistry, *J. Chem. Phys.*, 2013, **138**(3), 034703.

48 F. Tian, M. D. Radin and D. J. Siegel, Enhanced charge transport in amorphous Li$_2$O$_2$, *Chem. Mater.*, 2014, **26**(9), 2952–2959.

49 C. Ling, R. Zhang and K. Takechi, *et al.* Intrinsic Barrier to Electrochemically Decompose Li$_2$CO$_3$ and LiOH, *J. Phys. Chem. C*, 2014, **118**(46), 26591–26598.

29866 | *Phys. Chem. Chem. Phys.*, 2015, **17**, 29859–29866

This journal is © the Owner Societies 2015